

RESEARCH

Open Access



# Optimizing scenarios of a deep geothermal aquifer storage in the southern Upper Rhine Graben

Ingrid Stober<sup>1\*</sup>, Martin Jäggle<sup>2</sup> and Thomas Kohl<sup>3</sup>

\*Correspondence:

ingrid.stober@minpet.uni-freiburg.de

<sup>1</sup> Institute of Earth and Environmental Sciences, University of Freiburg, Albertstr. 23B, 79104 Freiburg, Germany

<sup>2</sup> Fraunhofer-Institut Für Physikalische Messtechnik IPM, Georges-Köhler-Allee 301, 79110 Freiburg, Germany

<sup>3</sup> Geothermics and Reservoir Technology, Karlsruhe Institute of Technology, Adenauerring 20B, 76131 Karlsruhe, Germany

## Abstract

Based on a newly developed geological 3D reservoir model for the demonstration site of the 'Freiburger Bucht' in the Upper Rhine Graben (SW Germany), geothermal development and realization concepts of an aquifer thermal energy storage (ATES) in the Buntsandstein aquifer were elaborated and energetically evaluated by numerical modeling. The thermal–hydraulic coupled modeling was performed with the FE-software OpenGeoSys and COMSOL. For this purpose, the geological model was converted into a numerical model and calibrated by local and regional, hydrogeological and geothermal measured values. A detailed study based on two-phase storage-heating cycles per year with constant injection temperature on the 'hot side' of the ATES, different volumetric flow rates, and temperature spreads was performed to quantify possible storage capacities, energies, and efficiencies. The calculated efficiency of the cyclic storage operation in this study, averaged over 10 storage heating cycles, are between 50 and 85%, depending on flow rate and temperature spread. The efficiency of the individual storage heating cycles increases from year to year in all scenarios considered, as the 'hot side' of the storage heats up in the long term. To increase ATES' efficiency, also horizontal wells were integrated into the numerical model and the results were compared with those of inclined wells.

## Introduction

Aquifer Thermal Energy Storage (ATES) is a reasonable method, to balance the seasonal offset and mismatch between thermal energy demand and supply (Doughty et al. 1982; Dincer 2002; Dickinson et al. 2009; Kranz and Frick 2013; Stober and Bucher 2021). This system is characterized by high storage efficiencies and high storage capacities and is therefore the preferred choice for long-term thermal energy storage (Lee 2010; Caliskan et al. 2012; Li 2016; Gao et al. 2017; Fleuchaus et al. 2018; Stricker et al. 2020). ATES is an open-loop systems, in which heat and cold is temporarily stored in the subsurface through injection and withdrawal of groundwater. Typically, the water heated up by surplus heat is injected during the summer months and produced back in winter (so-called storage cycle). Surplus heat is usually gained from combined heat and power plants, solar thermal energy systems, or waste. During the heating cycle (winter months) the

stored thermal energy is pumped back. In low-temperature ATES systems with  $T < 65$  °C, the pumped water may be heated additionally to meet the constant heat requirements of the district heating network (e.g., Kranz et al. 2022). However, if the ATES is used for heating greenhouses a large-scale heat pump may not be required (Middenmeer, Netherlands; Dinkelman et al. 2022).

Usually, aquifer thermal energy systems are subdivided into two groups: High Temperature ATES ( $T > 100$  °C) and Low Temperature ATES ( $T < 100$  °C). Generally, it is more efficient to store higher temperatures in the ATES because that improves heat pump performance (Wesselink et al. 2018; Bloemendal et al. 2022). However, in most countries warm well injection temperature of near surface ATES systems is limited to  $\leq 25$  °C or 30 °C (Haehnlein et al. 2010). This does not apply to deeper aquifers, significantly below potentially usable drinking water horizons, especially if they are separated from each other by low conductive layers. Due to its high storage capacities, ATES is most suitable for large-scale applications. These systems are usually designed to deliver base-load heat capacity, while peaks are delivered from other facilities, usually peak (gas) boilers. However, ATES application requires the presence of an aquifer and suitable hydrogeological conditions such as a low groundwater flow, high permeabilities, and suitable geochemical conditions (Schmidt and Müller-Steinhagen 2005; Fleuchaus et al. 2018; Dinkelman and van Bergen 2022).

Generally, reservoir permeability and thickness have a major impact on injection and production rates at compatible reservoir pressures and thus on ATES economics. Inclined wells or also deflected horizontal wells are a possibility to extend the filter section length in the reservoir drastically compared with vertical wells, and thus help to achieve higher rates at lower reservoir pressures (Bloemendal and Hartog 2016; Eren and Polat 2019).

First analytical and numerical simulations and comparison with field data already date back to the 1970s and 1980s (Rabbinov et al. 1971; Doughty et al. 1982; Sauty et al. 1982). However, the theoretical techniques at that time were not yet so far developed to model the more complex and dynamic processes in the subsurface as they were in later years. Nevertheless, since this time many ATES systems have been successfully installed in North America, China, and Europe, especially in the Netherlands (Dickinson et al. 2009). However, ATES are hardly known in numerous other countries. According to Bloemendal and Hartog (2016), well design of about 70% of Dutch ATES systems is suboptimal, because the effect of groundwater flow on efficiency and the effect of well design on subsurface space use was disregarded. In recent years, computer technology and numerical methods have advanced dramatically, so that a number of numerical codes, like TOUGH family, TIGER in MOOSE, OpenGeoSys, and COMSOL have been developed, which are capable of modeling the coupled thermal, hydraulic, mechanical, and chemical processes (THMC) (Stephanson 2004; Guimarães et al. 2006; Kolditz et al. 2012; Gholami Korzani et al. 2020; Permann et al. 2020; Dashti et al. 2023).

In this study, the 'Freiburger Bucht' (Fig. 1), we investigate the quantification of ATES potential by varying operating scenarios at the potential project site at the Fraunhofer IPM, situated in Freiburg (Germany) in the southern Upper Rhine Graben, topographically connected to the 'Freiburger Bucht' (Fig. 1). The aquifer examined here is about 700 m below surface and has an extremely low flow velocity. Modeling the coupled

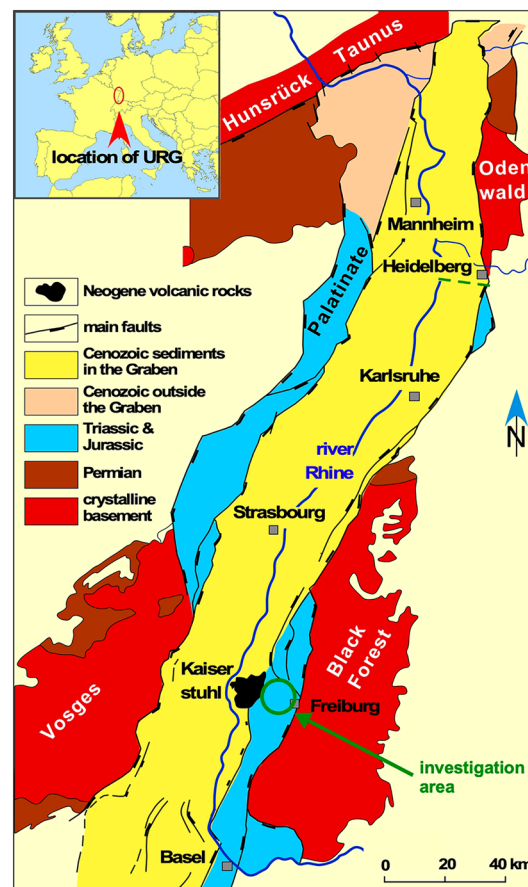


**Fig. 1** Schematic geological map of the Upper Rhine Graben (after Stober and Bucher 2015) showing the location of the investigation area

thermal and hydraulic processes (TH) was carried out with two different numerical 3D subsurface models (OpenGeoSys, COMSOL), both relating on the local geological, tectonic, and hydrogeological parameters. By varying temperature spread, injection- and production rate, and the configuration of the boreholes we infer to optimal conditions for realization of an aquifer thermal energy storage in the ‘Freiburger Bucht’.

Used software and copyright owners are listed in a separate section.

### Geological setting

The Upper Rhine Graben (URG), central part of the European Cenozoic Rift System, is approximately 300 km long and 30 to 40 km wide and has a laterally highly variable tectonic setting (Frey et al. 2022). In the southern and central part of the URG the main strike direction is NNE–SSW and in the northern part roughly N–S. The structure is bounded to the north by the Hunsrück and Taunus, to the south by the Swiss Jura Mountains near the town Basel and at the graben shoulders by the Black Forest, the Vosges, the Odenwald and the Palatinate (e.g., Illies and Fuchs 1974; Ziegler 1992; Dèzes et al. 2004; Rupf and Nitsch 2008) (Fig. 1).

The considered project site at the IPM (Fraunhofer-Institut für Physikalische Messtechnik) is situated in the SE part of the URG, within the so called Freiburger Bucht,

which is bounded by the Kaiserstuhl in the W and the Black Forest in the E (Figs. 1, 2). The tectonic situation within the ‘Freiburger Bucht’ is very complicated (Groschopf et al. 1996; Villinger 1999). The main inner graben fault of the URG with a vertical offset of about 3000 m crosses the Kaiserstuhl, an extinguished Miocene volcano. Approximately parallel extends the outer graben fault at the foot of the crystalline basement rocks of the Black Forest, showing a vertical offset of around 1500 m (e.g., Geyer and Gwinner 2011; Homilius and Schreiner 1991; Villinger 1999 and literature therein) (Fig. 2). The project site is situated between these large fault zones within a foothill zone of the Black Forest, largely covered with Quaternary and Pleistocene sediments. However, the foothill zone is subdivided into several small graben and horst systems. Some of these horsts consisting of Triassic, Jurassic, and Tertiary rocks are even elevated above ground level (e.g., Tuniberg, Lehener Bergle, Nimberg, Fig. 2). The geological sequence at the project site is shown in Fig. 3.

## Material, methods, and data

### Large-scale subsurface model of the ‘Freiburger Bucht’

The Petrel platform of Schlumberger was utilized by Jägge et al. (2018) to construct a large-scale subsurface model of the ‘Freiburger Bucht’ (Fig. 4), to get a better understanding of the complex geological and tectonic structure of the subsurface in the ‘Freiburger Bucht’. This model had a lateral extension of 8.4 km × 8.2 km and ended in 1500 m depth, well within the crystalline basement rocks. Due to the absence of seismic investigations in this area, the construction of the model is mainly based on deep wells and geologically interpreted, geoelectric deep-sounding 2D-sections, carried out throughout the ‘Freiburger Bucht’ (location given in e.g., Homilius and Schreiner 1991). Thus, geological 2D-cross-sections existed based on these

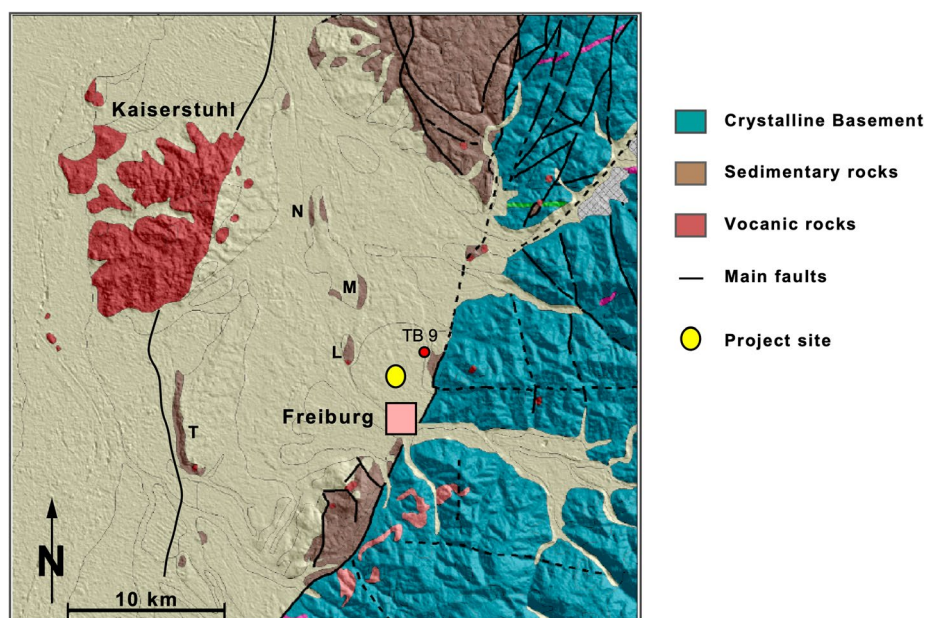


**Fig. 2** ‘Freiburger Bucht’ between Kaiserstuhl and Black Forest, showing the project site north of the town Freiburg. T-Tuniberg, L-Lehener Bergle, M-Marchhügel, N-Nimberg. TB 9-thermal well Zähringen (geological map after Groschopf et al. 1996)

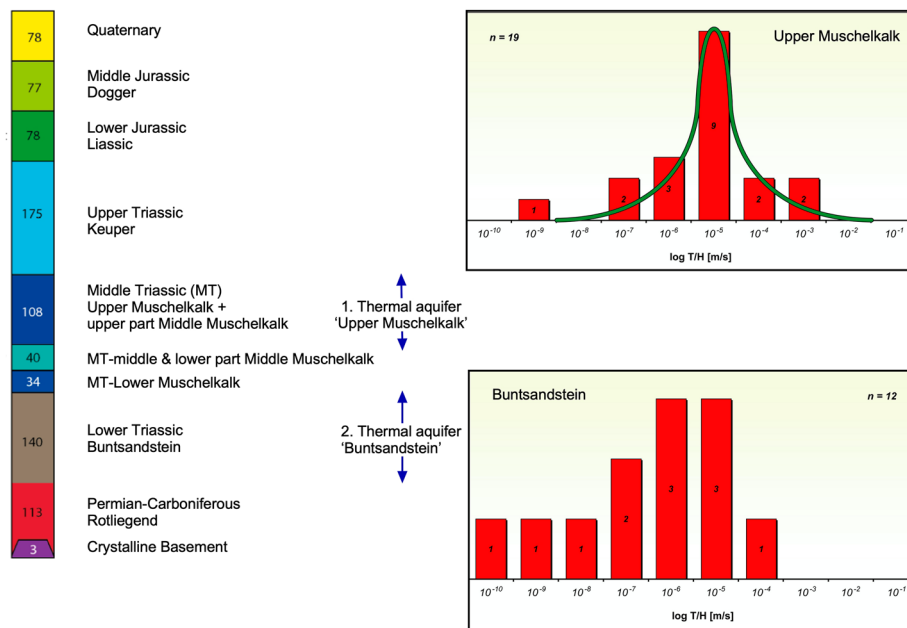


**Fig. 3** Schematic geological profile of the thermal well Zähringen TB 9, showing the two main thermal aquifers Upper Muschelkalk and Buntsandstein; hydraulic conductivity of the two thermal aquifers in the URG from Stober and Jodocy (2009)

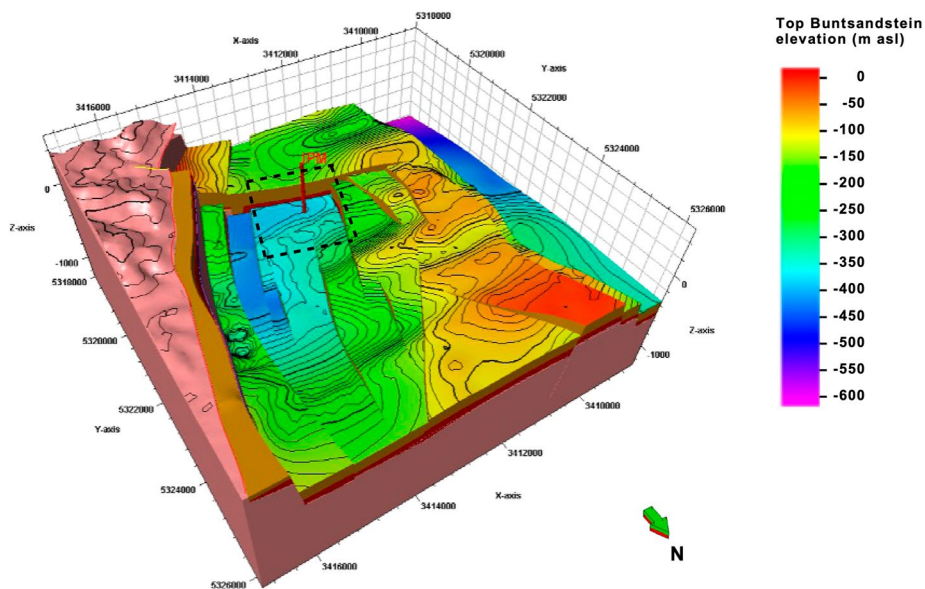


**Fig. 4** Large-scale geological-tectonic model of the 'Freiburger Bucht' between the Black Forest in the E (left side) and horst structures in the W (Lehener Berge, Marchhügel, Nimberg, Fig. 2) (right side). The figure shows depth of top Buntsandstein (in m asl) and the prominent 'Zähringer Graben' (light blue colors, in the center). The 'black dotted' line shows the location of the numerical 3D-model

geoelectric sections, published and documented in Groschopf et al. (1996), Villinger (1999), and Jodocy and Stober (2010). However, some of the cross sections were fraught with uncertainties and had to be re-interpreted by Jäggle et al. (2018). To build

up the geologic-tectonic model Jäggle et al. (2018) further used 47 wells with > 200 m depth and about 100 wells < 200 m (location of wells: Villinger 1999; Jodocy and Stober 2010; Jäggle et al. 2018). Only one borehole, the thermal well Zähringen TB 9 north of Freiburg, reached crystalline basement rocks at 846 m depth. TB 9 is in close vicinity of the project site and was used to derive the thickness of the individual layers in the large-scale subsurface model (Figs. 2, 3).

#### Hydraulic and thermal data used in the 3D-models

The geothermal and hydrogeological parameterization of the subsurface model is based on data of existing deep boreholes in the ‘Freiburger Bucht’ and is supplemented by data of the southern URG if necessary. However, only few deep boreholes, like the thermal well Zähringen TB 9 (Figs. 2, 3) or the wells of the spa Freiburg, exist in the ‘Freiburger Bucht’. The subsurface temperature in the model is based on temperature data of the southern Upper Rhine Graben. Schulz and Schellschmidt (1991) provide corrected subsurface temperatures for 75 boreholes, which were determined from production tests, bottom hole temperatures, temperature logs and heat flux density measurements. For the southern Upper Rhine Graben down to a depth of 800 m a mean temperature gradient of  $47 \text{ K km}^{-1}$  is obtained, leading to  $41.6 \text{ °C}$  temperature in the mean depth of the Buntsandstein ( $-450 \text{ m asl}$ ) at the project site. In accordance with measured data in the URG and in the ‘Freiburger Bucht’ (Stober and Jodocy 2009; Stober and Bucher 2015), hydraulic parameters were integrated in the numerical model (Fig. 3). The main input parameters of the numerical model are described and appropriately classified in Table 1, whereas fluid’s density  $\rho$  ( $\text{kg m}^{-3}$ ) and viscosity  $\mu$  ( $\text{kg m}^{-1} \text{ s}^{-1}$ ) are variables depending on temperature and pressure.

#### Design of the 3D-numerical subsurface model for heat storage with the softwares OpenGeoSys and COMSOL

The large-scale geological model of the ‘Freiburger Bucht’ (Fig. 4) was used to construct the significantly smaller, numerical 3D-model (location shown in Fig. 4), in which the

**Table 1** Overview of the main formation and fluid parameters used in the numerical model

Formation	Muschelkalk	Buntsandstein	Top; bottom; intermediate	Fault	Well
Dimension	3	3	3	2	1
Porosity (—)	0.05	0.05	0.01	0.2	1
Permeability ( $\text{m}^2$ )	$5.74 \times 10^{-13}$	$8.20 \times 10^{-14}$	$8.20 \times 10^{-16}$	$1.00 \times 10^{-10}$	1.0
Density ( $\text{kg m}^{-3}$ )	2680	2200	2600; 2700; 2680	2600	1000
Specific heat capacity ( $\text{J kg}^{-1} \text{ K}^{-1}$ )	675	700	675; 750; 675	850	4193.5
Therm. conductivity ( $\text{W m}^{-1} \text{ K}^{-1}$ )	2.0	2.5	2.1; 2.3; 2.0	2.2	0.65
Fluid					
Specific heat capacity ( $\text{J kg}^{-1} \text{ K}^{-1}$ )	4193.5				
Therm. conductivity ( $\text{W m}^{-1} \text{ K}^{-1}$ )	0.65				

The stratigraphic subdivisions of the top, bottom and intermediate units are shown in Fig. 5. Fluid parameters density  $\rho$  ( $\text{kg m}^{-3}$ ) and viscosity  $\mu$  ( $\text{kg m}^{-1} \text{ s}^{-1}$ ) are variables depending on temperature and pressure

so-called Zähringer Graben is located in the central area (Fig. 5). This numerical sub-model is bounded by fault zones in the E and W and has a lateral extension of c. 2.5 km in NNE-SSW direction and of c. 2.2 km in ESE-WNW direction. The depth range is 1.15 km (250 m–900 m asl). To optimize the FE mesh, the numerical 3D-model is reduced to 5 layers containing only the principal lithological and hydraulic settings and properties of the large-scale geological model, shown in Fig. 5. It thus comprises the two thermal aquifers (Upper Muschelkalk, Buntsandstein), a low-permeable intermediate layer in between (lower part of Middle Muschelkalk—Lower Muschelkalk), the top layer (Upper Mesozoic—Quaternary), and the bottom layer (Permian, Crystalline Basement) (Fig. 5, Table 1).

The project site of the Fraunhofer IPM is situated within the so-called 'Zähringer Graben' (Fig. 4) at the foot hill zone of the Black Forest, which is bounded in the W by nearly N–S oriented horst structures (Lehener Bergle—Nimberg, Fig. 2) and in the E by the outer graben fault, i.e., by basement rocks (Fig. 4). The 'Zähringer Graben' is broader in the S (ca. 4.5 km) than in the N (ca. 3 km) of the model area. S of the project site, a E–W oriented fault crosses the 'Zähringer Graben' (Fig. 4), but neither length, age, nor hydraulic character are known (Villinger 1999; Groschopf et al. 1996). At the project site (ca. 250 m asl), top Mesozoicum is expected at –120 m asl, Top Muschelkalk at –440 m asl, top Buntsandstein at –620 m asl, and top basement at –855 m asl. The thermal aquifers of the Upper Muschelkalk and the Buntsandstein are suitable as deep aquifer thermal energy storage (ATES). The 'Upper Muschelkalk aquifer' includes parts of the lower Keuper and of the upper Middle Muschelkalk. Both thermal aquifers are already used in several spas (e.g., Bad Krozingen, Freiburg) or geothermal plants in the URG (Riehen, Rittershoffen, Bruchsal).

The significantly smaller, numerical 3D-model was constructed to carry out different reservoir storage simulations with varying rates (5, 10, 20, 30, 40 L s<sup>-1</sup>) and temperature spreads ( $\Delta T = 30$  K; 38.4 K; 50 K). Numerical computation was done using the open-source software OpenGeoSys, a finite element code for simulating thermal–hydraulic–mechanical–chemical (THMC) coupled processes in fractured-porous media (Kolditz et al. 2012). The same 3D-model was used subsequently in the application of the commercial computer program COMSOL Multiphysics (termed COMSOL throughout the text), a finite element analysis, solver, and simulation software package. We compared the results from the OpenGeoSys and the COMSOL computations

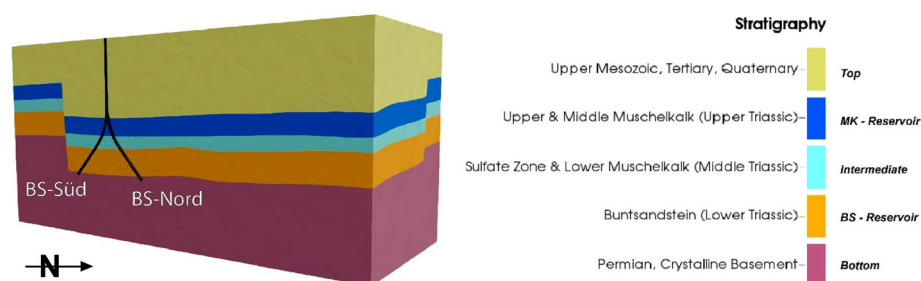


**Fig. 5** Cross section through the 3D model (location in Fig. 4) with the used simplified stratigraphy, showing the position of the geothermal doublet

with each other and additionally carried out variations in borehole configuration with COMSOL. Mechanical and chemical variations were not considered in both applications. The idealized geometry and the structural geological elements were discretized with a three-dimensional computational mesh using the program MeshIt (Cacace and Blöcher 2015). The FE-mesh, locally refined in vicinity of the boreholes, thus consisted of 3D tetrahedra for rock matrix, 1D-polylines for the filter sections of the doublet, and 2D-triangulated surfaces for the faults (Table 1). The optimal FE grid size was determined via a sensitivity analysis. For details concerning the sensitivity analysis see Jägge et al. (2018). The discretizing mesh size for the numerical model was spatially distributed as follows: 2 m, 64 m, and 128 m at the well, reservoir or fault, and other stratigraphic units, respectively. Thus, the total model consists of about 200,000 FE-cells. The discretization in time applied time steps ranged between  $10^3$  s at the beginning of each storage- and heating-cycle and  $10^6$  s towards the end of the cycle. This discretization resulted in a very stable numerical simulation (without any fluctuations) of the numerical 3D-model with the simulation software OpenGeoSys (and later with the software COMSOL). A significant influence of the spatial mesh size configuration as well as of the meshing gradients on the modeling results could not be identified. Maximum deviations in temperature values vary only by 0.01–0.1 K and in pressure values only in the order of  $10^4$ – $10^5$  Pa.

Due to its greater thickness and higher temperature, the Buntsandstein aquifer was chosen as a potential ATEs site with seasonal storage and production of heat. This also avoided conflicts with the spa of Freiburg, which is using the Upper Muschelkalk aquifer. Thus, the lithological structure of the numerical concept model is suitable for the planned simulations.

In the OpenGeoSys-model the c. 150 m thick Buntsandstein aquifer is intersected by the hydrothermal doublet between –370 and –520 m asl. Distance between the two boreholes at the top of the Buntsandstein is 200 m and at the base of the wells 500 m. In this configuration, the filter section of the wells has a length of c. 210 m (Fig. 5). In the COMSOL-modeling the same doublet configuration is used, but additionally computations with horizontal wells of different lengths and distances are carried out.

### **Influence of well design**

Figure 6 shows different well configurations with longer filter sections in the aquifer. However, there are a lot of other possibilities (e.g., Stricker et al. 2020). Configuration A, inclined wells, is used in the OpenGeoSys-model (Fig. 5), whereas in the COMSOL model additionally horizontal wells are implemented. Figure 6 shows two different configurations for horizontal wells (B, C). Long horizontal wells have the hydraulic advantage of lowering the differential pressure induced by production/injection. The advantage of configuration B is, that it is possible to drill both horizontal wells from a single platform, in contrast to configuration C. However, even in configuration C it is still possible to drill both wells from one site, but then relatively complex borehole path geometries are necessary. Configuration C has a hydraulic advantage. In long horizontal wells induced pressure might drop along the length of the horizontal section, leading to irregular flow distribution along the horizontal filter sections. Shiozawa and McClure



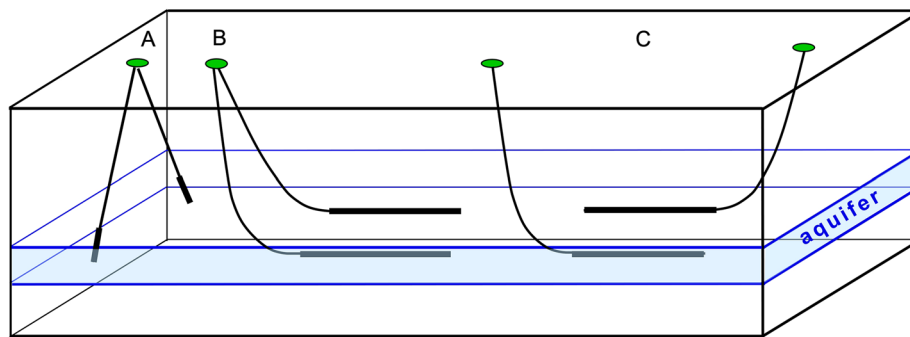


**Fig. 6** Different possible well configurations. Filter sections in all configurations are in the aquifer (light blue) indicated by 'bold black lines'. **A** Inclined wells. **B** Horizontal wells drilled from a single drilling site. **C** Horizontal wells drilled from two drilling sites

(2014) have shown that with configuration C potentially irregular outflow from the filter section into the reservoir (resp. inflow into the horizontal well) can be reduced or even avoided and connection between the two wells improved by the different arrangement of the wells (configuration C) in the aquifer. Thus, for practical implementation configuration C is recommended.

To be more flexible for future use, the earlier 3D-model based on OpenGeoSys simulations, was implemented in the commercial computer program COMSOL. The temperature dependent values for the dynamic viscosity, thermal conductivity, density and heat capacity of the fluid were taken from the COMSOL material database for water. In the COMSOL-model three different filter section lengths of the two parallel horizontal wells (250 m, 500 m, 1000 m) and different distances between the horizontal wells in the aquifer (100 m, 400 m) for all well configurations are integrated. Filter sections are based on 8" boreholes with a maximum mesh size of 0.1 m. Horizontal filter sections were parametrically modelled in a depth of -450 m asl. The influence of varying production- and injection rates ( $10 \text{ L s}^{-1}$ ,  $40 \text{ L s}^{-1}$ ,  $100 \text{ L s}^{-1}$ ) on pressure drawdown and pressure buildup are investigated for all scenarios. Hydraulic friction along the length of the horizontal section is not taken into account within this investigation.

#### Heat power of the aquifer storage

The heat power ( $P$ ) of the aquifer storage depends primarily on two factors: (i) the flow rate ( $Q$ ) chosen for the injection and production of water into and from the reservoir; (ii) the temperature spread ( $\Delta T$ ) chosen for heat extraction by the heat exchanger in the heating plant (reinjection temperature at the 'cold side' of ATEs):

$$P = \rho c_p Q \Delta T \left( \text{J s}^{-1} \text{ or W} \right) \quad (1)$$

with  $\rho$  ( $\text{kg m}^{-3}$ ) density and  $c_p$  ( $\text{J kg}^{-1} \text{ K}^{-1}$ ) heat capacity of water; both parameters are dependent on temperature and pressure.

The technical–economic balancing of a cyclic underground storage operation is carried out via scenario-based individual models. In these individual models, the input

parameters are modified, either to represent different modes of storage operation or to quantify the influence of uncertainties in the hydrogeological input parameters.

## Results

The initial, undisturbed thermal and hydraulic state of the 'Freiburger Bucht' served as start model for the transient thermo-hydraulic (TH) ATEs simulation with the cyclic reservoir management. This steady state model was calibrated using known temperature and pressure measurements. First computations were carried out with OpenGeoSys, later ones with COMSOL.

### Engineering economics of the cyclic storage and heating operation with the software OpenGeoSys

The *reference model* for the model comparisons is based on the input parameters from Table 1 and considers a constant flow rate of  $Q = 10 \text{ L s}^{-1}$  and a temperature spread of 30 K. Aquifer storage operation is considered as a two-cycle process, with a storage cycle and a heating cycle. During the storage cycle, water heated up to a constant temperature of 80 °C is pumped into the reservoir via the well BS-North ('hot side' of ATEs), whereas the required low-temperature water is taken from the reservoir via the well BS-South ('cold side' of ATEs) (Fig. 5). Thus, the amount of energy stored in the reservoir depends on the water temperature pumped out of BS-South. During the heating cycle, the polarity of the doublet is reversed, i.e., the former injection well BS-North becomes the production well and vice versa. Reinjection of the water into BS-South takes place under constant injection temperatures of 50 °C, i.e., with a temperature spread of  $\Delta T = 30 \text{ K}$ . Thus, the amount of energy extracted depends only on the produced temperature values. Both phases last 175 days each at constant pumping rates. Between the two phases there is a 7.5-day rest period without pumping activity. Figure 7 gives an overview of the storage operation based on the resulting reservoir pressures.

### Effect of temperature and rate variations on pressure- and temperature distribution in the aquifer

Permeability, production rate, and pressure drawdown are dependent on each other. If permeability is very low the production rate will be low too at a comparatively high pressure drawdown. Very low permeabilities result in an uneconomic project. In our numerical modeling permeability was always constant (Table 1). However, to accommodate the influence of permeability variations on economics, we varied the production- and injection rates. Increasing the permeability by 100% would lead approximately to a halving of the maximum differential pressures (pressure drawdown) and a reduction of permeability to 50% would lead to an approximate doubling of the maximum differential pressures (pressure drawdown). Magnitude and location of the generated temperature anomalies at the wells BS-North and BS-South in cyclic reservoir operation is independent of reservoir permeability.

In a first scenario the influence of *varying production- and injection rate (Q)* on pressure within the Buntsandstein aquifer is investigated. Figure 8A and B shows that changing production- and injection-rate between 5 and 40  $\text{L s}^{-1}$  will lead to an increase of maximal pressure differences from 2 bar up to 14 bar. Generally, it can

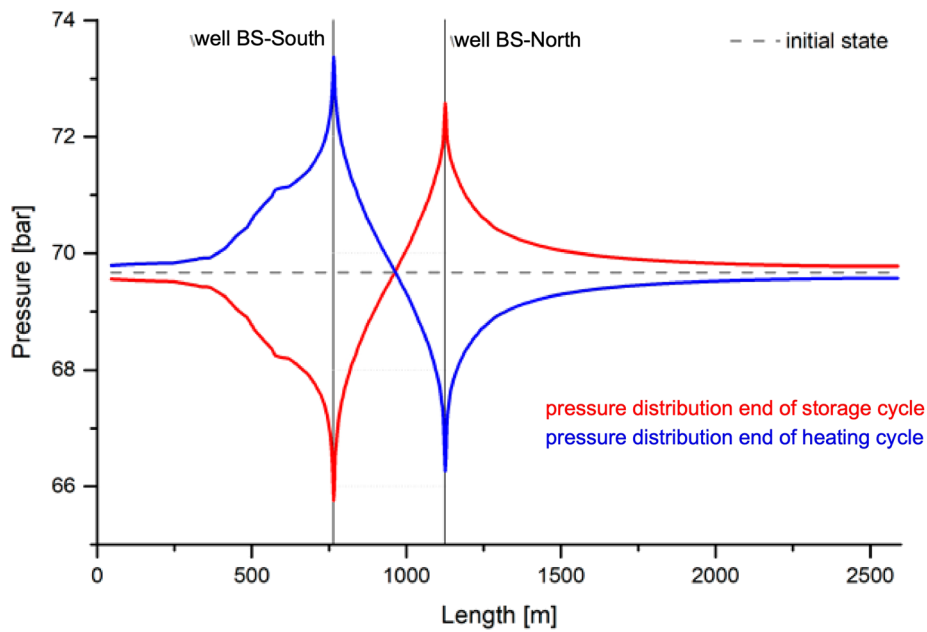


**Fig. 7** Pressure distribution in the Buntsandstein aquifer at the end of the storage cycle after 175 d injection of heated water (80 °C) into the well BS-North and production via well BS-South (red line); rates  $Q = 10 \text{ L s}^{-1}$ . The 'blue line' refers to the pressure distribution in the same aquifer at the end of the heating cycle, i.e., production from well BS-North and injection of colder water (50 °C) into BS-South. Please note the influence of the fault in vicinity of the well BS-South (Fig. 5) on pressure distribution in the aquifer

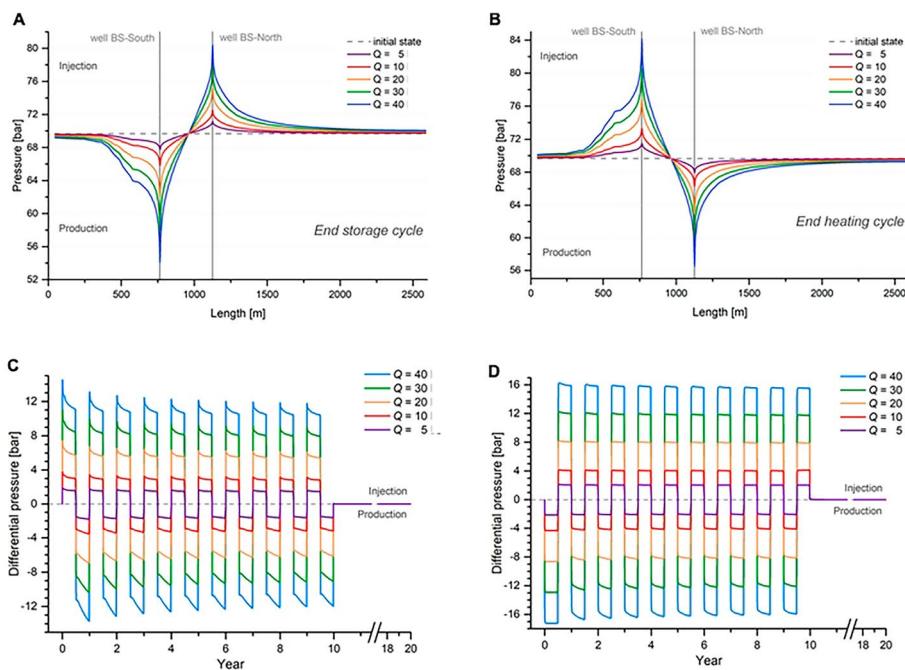


**Fig. 8** Comparison of pressures in the N-S section through the Buntsandstein aquifer at the end of a 175 d storage cycle (A) and heating cycle (B) based on varying injection rates of 5, 10, 20, 30, and  $40 \text{ L s}^{-1}$ . Comparison of long-term behavior of differential pressures in the Buntsandstein aquifer over 10 storage and heating cycles at wells BS-North (C) and BS-South (D) based on varying injection rates of 5, 10, 20, 30, and  $40 \text{ L s}^{-1}$

be stated that the pressure response of the reservoir between heating and storage cycles are proportionally related. Pressure differences in well BS-South are slightly higher than in well BS-North due to a nearby fault (Fig. 5). The long-term behavior (10 storage-heating cycles) of the reservoir pressure is stable, regardless of the flow rate (Fig. 8C, D). At higher flow rates, an initial pressure peak becomes evident at the beginning of each pumping cycle, especially at BS-North. Towards the end of each pumping cycle, the differential pressures tend towards steady-state pressure conditions. Due to slightly increasing reservoir temperatures and thus lower fluid densities and viscosities, the differential pressures decrease slightly during the course of the long-term operation.

Increasing the flow rate from  $5 \text{ L s}^{-1}$  up to  $40 \text{ L s}^{-1}$  will lead to an increase of the diameter of the temperature change at the end of the first storage cycle -based on the 1 K isotherm- from approx. 150 m to approx. 350 m. With the selected doublet geometry, a minimal thermal breakthrough is already evident at a flow rate of  $40 \text{ L s}^{-1}$  (Fig. 9). Since homogeneous and isotropic reservoir properties and no natural groundwater movement were assumed in this scenario, the generated temperature anomalies are approximately symmetrical.

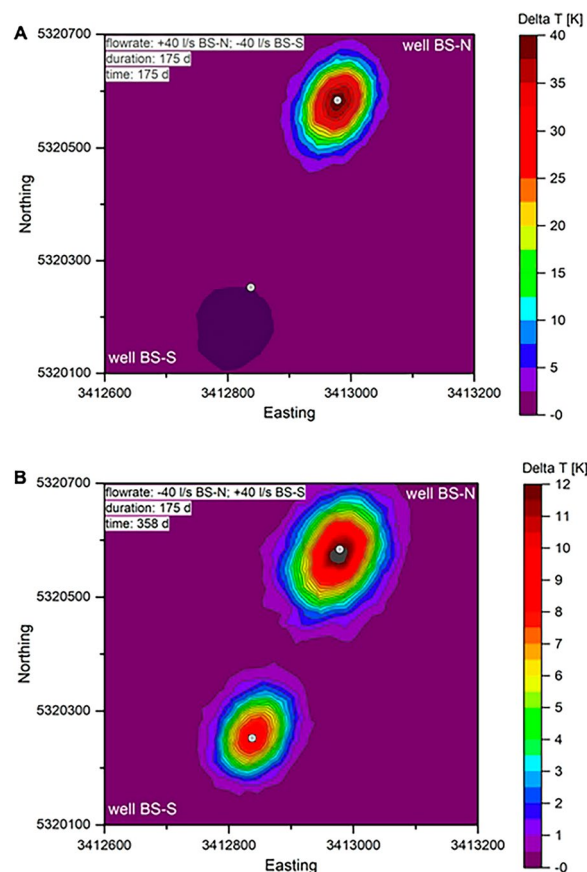


**Fig. 9** Comparison of temperature changes in a horizontal section through the aquifer at the end of a 175 d storage cycle (A) and heating cycle (B), based on a flow rate of  $40 \text{ L s}^{-1}$  and constant injection temperature of  $80 \text{ }^\circ\text{C}$  in well BS-North (storage cycle) and  $50 \text{ }^\circ\text{C}$  in well BS-South (heating cycle). Please note the change in temperature scaling between storage and heating cycles

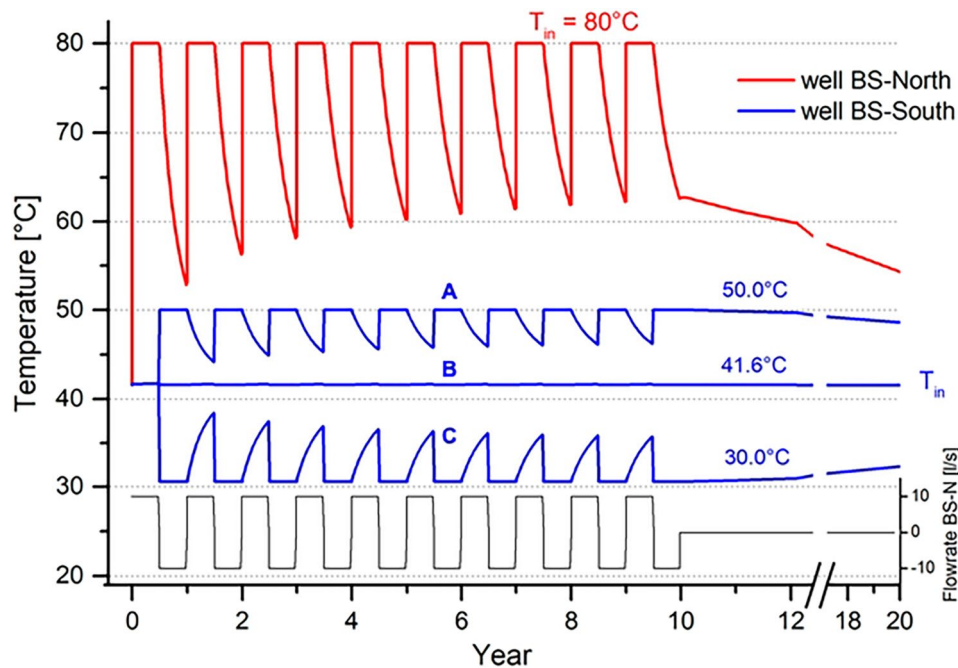


**Fig. 10** Long-term behavior of the aquifer temperature in close vicinity of the wells BS-North (red) and BS-South (blue) at 3 different heat extractions in the heating cycle. Flow rate ( $Q = 10 \text{ L s}^{-1}$ ) and injection temperature ( $80^\circ\text{C}$ ) during storage cycle are constant. At the ‘hot side’ of the aquifer storage temperature is increasing with each cycle (red). Influence of storage efficiency on the ‘cold side’ of the aquifer storage is shown by 3 scenarios (A, B, C)

In a second scenario the influence of *varying temperature spread* ( $\Delta T$ ) on temperature distribution within the aquifer is investigated, whereas injection temperature during the storage cycle as well as production-/injection rate are constant ( $80^\circ\text{C}$ ;  $Q = 10 \text{ L s}^{-1}$ ). Three different operation modes, i.e., three different temperature spreads ( $\Delta T = 30 \text{ K}$ ;  $38.4 \text{ K}$ ;  $50 \text{ K}$ ), are investigated, which are during the heating cycles corresponding to injection temperatures in well BS-South (‘cold side’ of ATEs):

- $50^\circ\text{C}$ , i.e., about  $10^\circ\text{C}$  higher than undisturbed reservoir temperature,
- $41.6^\circ\text{C}$ , equal to undisturbed reservoir temperature, and
- $30^\circ\text{C}$ , about  $10^\circ\text{C}$  below undisturbed reservoir temperature.

The amount of injected surplus heat during the storage cycle results from the constant flow temperature of  $80^\circ\text{C}$  and the temperature of the pumped thermal water from well BS-South, the ‘cold side’ of the aquifer storage.

Figure 10 shows the long-term behavior (10 storage and heating cycles) of temperature in the reservoir for different heat extractions, i.e., different temperature spreads.

During the storage cycle  $80^\circ\text{C}$  hot water is injected with a constant rate of  $10 \text{ L s}^{-1}$  via well BS-North into the Buntsandstein aquifer, which has an undisturbed temperature of  $41.6^\circ\text{C}$ . Afterwards, in the heating cycle, water is again pumped out of the aquifer via well BS-North. Temperature of the pumped water is decreasing, in the first cycle from  $80^\circ\text{C}$  (injection-temperature) to  $53^\circ\text{C}$ . The figure also indicates, that in the course of the cyclic storage and heating operation, the temperature of the pumped water increases

after each heating cycle (e.g., 63 °C after the 10th cycle). This is the result of the continuous heating up of the aquifer in the surroundings of well BS-North ('hot side of ATES) and therewith an increasing temperature spread which yields an improving efficiency of the aquifer storage from year to year.

Figure 10 also shows the effect of three different injection temperatures (50 °C; 41,6 °C; 30 °C) in well BS-South, i.e., on temperature performance at the 'cold side' of the aquifer storage. Injection of water with a higher temperature than in the undisturbed aquifer, leads to a successive increase of temperature, i.e., temperature at the 'cold side' of the aquifer storage is increasing from cycle to cycle (A in Fig. 10). As a result, the realizable temperature spread during the storage cycle becomes slightly smaller from year to year and less energy can be stored in the 'hot side' of the aquifer storage. In contrast, injection of colder water than in the aquifer will lead to temperature decrease on the 'cold side' of the aquifer with the result, that slightly more energy can be stored in the aquifer (C in Fig. 10). Injection of water in well BS-South, with undisturbed aquifer temperature, will lead to constant energy storage conditions (B in Fig. 10).

#### ***Performance of the aquifer storage at different injection- and production rates and different temperature spreads***

The heat power ( $P$ ), i.e., the energetic withdrawal capacity, depends mainly on flowrate and temperature spread (Eq. 1). As shown in Fig. 10 temperature at production wells (BS-North, BS-South) changes during each heating- and storage cycle and from cycle to cycle, for temperature spread of 30 K and 50 K. Thus, the thermal power of the aquifer storage is not constant. We calculated the long-term performance of the aquifer storage (10 storage-heating cycles) for the three, before described operation modes, each with constant injection temperature of 80 °C in BS-North during storage cycles and varying injection temperature in BS-South during heating cycles (50 °C; 41.6 °C; 30 °C) based on different flow-rates (5, 10, 20, 30, 40 L s<sup>-1</sup>). Selected results for flow rate  $Q = 10 \text{ L s}^{-1}$  are shown in Fig. 11.

**Storage cycles** Regardless of temperature spread, the performance (given in thermal power, MW<sub>t</sub>) in the first storage cycle is constant, since constant temperatures are pumped from the BS-South ('cold side') in the first year. The heat storage power at the first storage phase is 0.8 MW<sub>v</sub>, 1.6 MW<sub>t</sub> and 6.5 MW<sub>t</sub> at flow rates of 5 L s<sup>-1</sup>, 10 L s<sup>-1</sup> and 40 L s<sup>-1</sup>, respectively. Figure 11 shows the heat storage power (1.6 MW<sub>t</sub>) for flow rate  $Q = 10 \text{ L s}^{-1}$ .

With a temperature spread of 30 K, performance of the storage cycle is decreasing in the course of the long-term operation of the aquifer storage, as increasingly warmer water is pumped from BS-South. This means that less surplus heat can be stored in the subsurface. The energetic withdrawal capacity at the beginning of the subsequent storage cycles drops to c. 1.25 MW<sub>t</sub> at flow rate 10 L s<sup>-1</sup>. However, it is increasing by c. 20% (c. 1.5 MW<sub>t</sub>) at the end of the single storage cycles (Fig. 11A). Contrarily, temperature spread of 50 K leads to an increase in the course of the long-term operation, as increasingly colder water is pumped from BS-South, i.e., more surplus heat can be stored in the subsurface and subsequently the performance of the storage cycle is increasing from 1.6 up to c. 2.0 MW<sub>t</sub> at the beginning of the storage

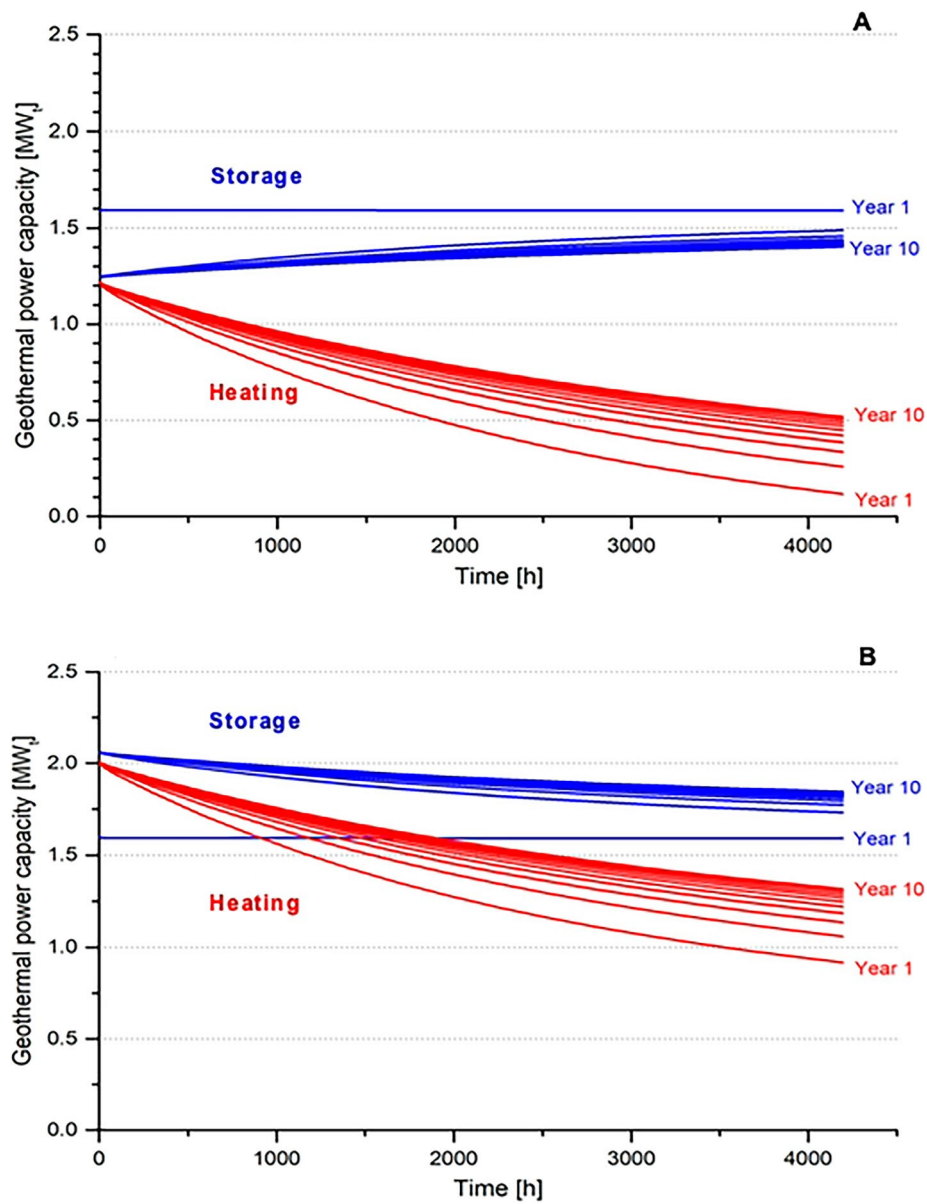


**Fig. 11** Long-term performance of the aquifer storage (given in geothermal power capacity,  $MW_t$ ) for two different temperature spreads  $\Delta T=30\text{ K}$  (**A**) and  $\Delta T=50\text{ K}$  (**B**), constant injection temperature of  $80\text{ }^\circ\text{C}$  in BS-North and flow rate of  $10\text{ L s}^{-1}$  (compare Fig. 10). Undisturbed aquifer temperature is  $41.6\text{ }^\circ\text{C}$

cycles at pumping rate of  $10\text{ L s}^{-1}$ . However, at the end of each storage cycle the performance is decreasing by 15–20% (Fig. 11B). With temperature spread of  $38.4\text{ K}$ , the performance of the storage phase is almost constant over 10 years, since the supply temperatures from well BS-South (‘cold side’ of ATES) are constant.

*Heating cycles* The geothermal heat production power of the initial heating cycles are at a temperature spread of:

- 30 K: between 0.6 MW<sub>t</sub> (5 L s<sup>-1</sup>) and 5.0 MW<sub>t</sub> (40 L s<sup>-1</sup>); at Q = 10 L s<sup>-1</sup>: 1.25 MW<sub>t</sub>
- 38.4 K: between 0.8 MW<sub>t</sub> (5 L s<sup>-1</sup>) and 6.4 MW<sub>t</sub> (40 L s<sup>-1</sup>); at Q = 10 L s<sup>-1</sup>: 1.6 MW<sub>t</sub>
- 50 K: between 1.0 MW<sub>t</sub> (5 L s<sup>-1</sup>) and 8.0 MW<sub>t</sub> (40 L s<sup>-1</sup>); at Q = 10 L s<sup>-1</sup>: 2.0 MW<sub>t</sub>

In general, the geothermal heat power decreases during each heating cycle as the thermal water temperatures extracted from the BS-North ('hot side') slowly decrease (Figs. 10, 11). Storage operation scenarios with high temperature spreads are characterized by lower drops during the heating cycle (Fig. 11B), which means that more energy can be extracted from the storage. However, the extent of the decrease is time dependent and decreases from year to year, causing higher production temperatures at the end of further heating cycles. Due to the continuous, irreversible heating of the 'hot side' of the aquifer storage temperature- and performance drop during the heating cycles is continuously reduced. Thus, regardless of the selected flow rate and temperature spread, slowly reduced performance-increases of the heating cycles are to be expected.

For the *energetic balancing*, stored and produced energies were calculated for each storage-heating cycle. Since the output of the aquifer storage is not constant due to variable temperature spreads, the stored and produced energies result from the integral of the output over 175 days each (summer- and winter operation). Table 2 gives an overview of the annually stored and produced energies for different scenarios.

The efficiency of an aquifer storage can be expressed by the *recovery factor*, which is calculated as quotient of energy produced to energy stored. The recovery factor does not account for losses in the borehole or heat exchanger. It is strongly dependent on the operation-scenarios of the ATES. Higher efficiencies are possible by either a prolongation of the heat extraction phase or by increasing the flow rate during the production period.

Calculations showed that the efficiency of the aquifer storage, i.e., the recovery factor, is predominantly determined by the selected temperature spread ( $\Delta T$ ), whereas the influence of flow rate changes the storage efficiency by only a few percentage points. Generally, the recovery factor, i.e., efficiency of an aquifer storage is increasing in the course of long-term operation. At the end of the long-term aquifer storage operation with the rate  $Q = 10 \text{ L s}^{-1}$  and three different temperature spreads ( $\Delta T$ ) recovery factors of 60% ( $\Delta T = 30 \text{ }^\circ\text{C}$ ), 72% ( $\Delta T = 38.4 \text{ }^\circ\text{C}$ ), and 82% ( $\Delta T = 50 \text{ }^\circ\text{C}$ ) result (Fig. 12). Higher rates lead to higher recovery factors. Highest efficiency is obtained with injection temperatures in BS-South ('cold side' of ATES), which are below the undisturbed aquifer temperature.

**Table 2** Mean values annually stored and produced energies (GWh) in the first 10 years of operation for different temperature spreads ( $\Delta T$ ), different injection-/production-rates, and constant injection temperature of 80 °C in well BS-North

Temperature spread ( $\Delta T$ )	Stored energy (GWh)			Produced energy (GWh)		
	Rate: 5 L s <sup>-1</sup>	Rate: 10 L s <sup>-1</sup>	Rate: 40 L s <sup>-1</sup>	Rate: 5 L s <sup>-1</sup>	Rate: 10 L s <sup>-1</sup>	Rate: 40 L s <sup>-1</sup>
30 K	2.9	5.8	22.5	1.5	3.2	13.0
38.4 K	3.3	6.9	26.7	2.2	4.9	18.8
50 K	4.0	8.0	32.0	3.1	6.8	26.3



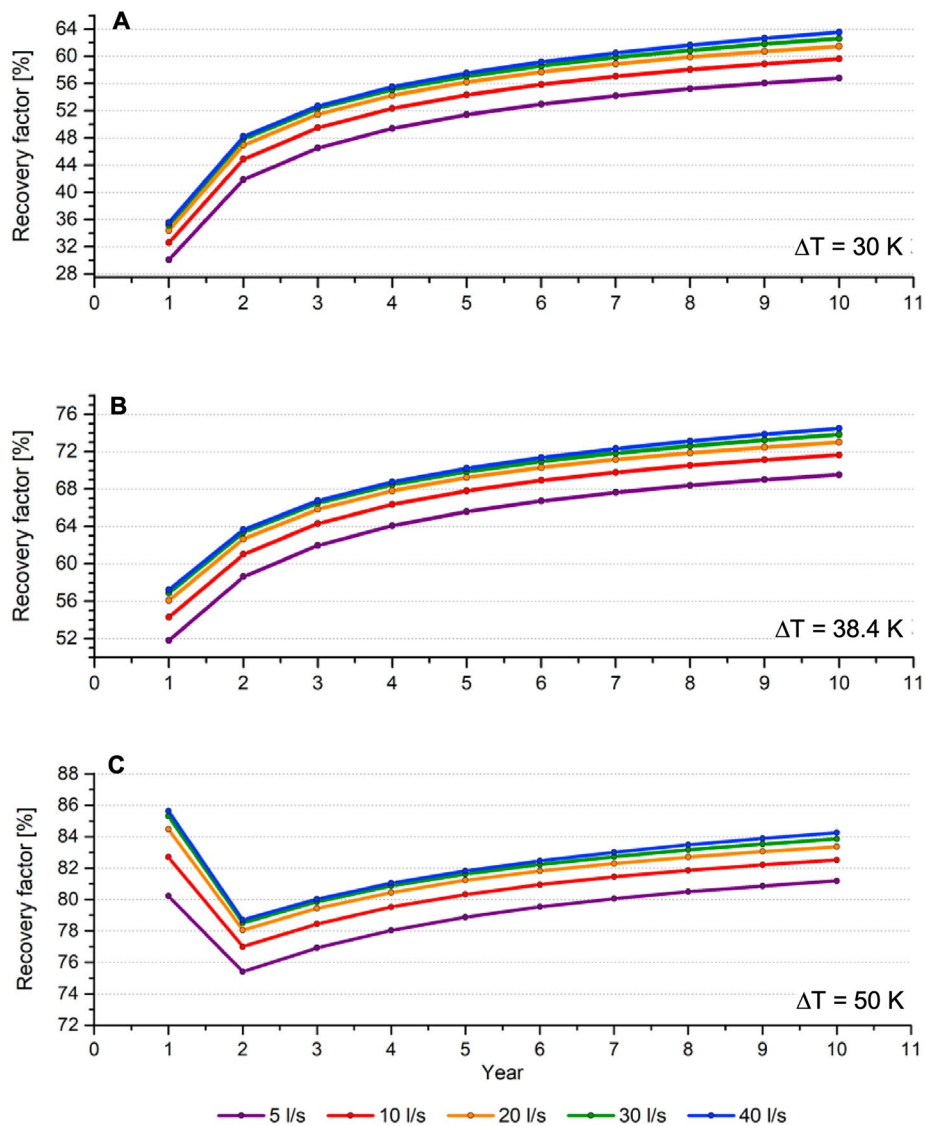


**Fig. 12** Efficiency of an aquifer storage (presented as recovery factor) over 10 years (10 storage-heating cycles), each with 175 d long storage and heating cycles per year. Flow rates of 5, 10, 20, 30 and 40 L s<sup>-1</sup> were considered in three different operating modes (temperature spreads ( $\Delta T$ ), each with constant injection temperature of 80 °C during the storage cycle, but with varying injection temperatures in the heating cycle of 50 (A), 41.6 (B) and 30 °C (C). Please note the different scales on the vertical axes

### Influence of different well configurations on the heat extraction rate using the COMSOL application

After successful calibration and validation, the simulations with different borehole geometries were performed with COMSOL. Permeability of  $8.2 \times 10^{-14} \text{ m}^2$  of the 150 m thick aquifer is relatively low to medium, thus even low injection and production rates ( $Q = 10 \text{ L s}^{-1}$ ) lead to pressure variations of up to  $\Delta p = 8 \text{ bar}$  (pressure difference between ‘cold’ and ‘hot side’ of ATEs) in the first operation cycle of the reference model, where inclined wells with filter section lengths of 210 m were implemented (Fig. 8). To increase injection- and production rate while maintaining low pressures, horizontal wells with different length of filter sections (and different

distances between the horizontal wells in the aquifer) are incorporated in the COM-SOL-model and pressure differences between the ‘cold’ and ‘hot side’ of the ATES calculated. The following results of these calculations show the pressure buildup and—drawdown at the end of the half a year lasting 1st storage cycle with injection of 80 °C hot water and at the just as long lasting 1st heating cycle with re-injection of water having more or less undisturbed aquifer temperature (Fig. 13A, B). This scenario was chosen, because highest pressure variations occur in the first cycles (Fig. 8).

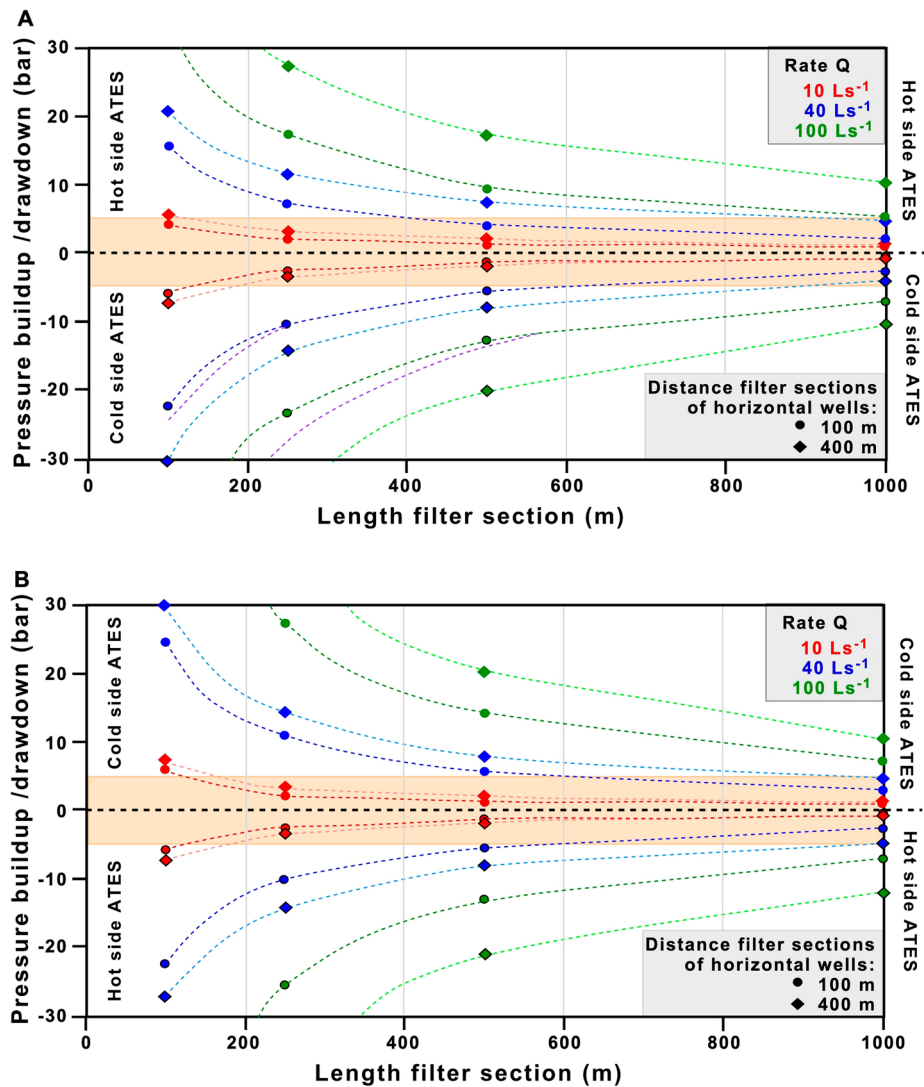


**Fig. 13** Pressure buildup and drawdown at the ‘hot’ and ‘cold side’ of ATES due to injection and production with different rates ( $10 \text{ L s}^{-1}$ ,  $40 \text{ L s}^{-1}$ ,  $100 \text{ L s}^{-1}$ ) in dependence of filter section length of the horizontal wells at the end of the first storage cycle (A) and at the end of the first heating cycle (B). The calculations were performed for 100 m and 400 m distance between the horizontal wells. The differential pressure marked ‘orange’ refers to gentle operation conditions

### **Storage cycle**

With increasing length of the horizontal wells' filter section both wells reduce pressure at the same flow rate. For example, at  $Q = 10 \text{ L s}^{-1}$ , 100 m distance between the two horizontal filter sections, and a filter section length ( $L$ ) of 250 m results in a pressure difference between the wells of  $\Delta p \approx 4.7$  bar, whereas  $L$  of 1000 m would reduce the pressure difference to only  $\Delta p \approx 0.7$  bar. Horizontal wells show generally low pressure-differences, e.g.,  $Q = 40 \text{ L s}^{-1}/L = 500$  m results in  $\Delta p \approx 5.6$  bar and  $Q = 100 \text{ L s}^{-1}/L = 1000$  m results  $\Delta p \approx 12.3$  bar. Generally, pressure changes at the 'hot side' of ATES are lower than at the 'cold side', because the dynamic viscosity of hot water is lower than of colder water (Fig. 13A). The numerical results show as well, when increasing the distance between the two filter sections of the horizontal wells (from 100 to 400 m), higher pressure changes—with respect to the undisturbed pressure—on the 'hot' and the 'cold side' of ATES result, because of lower hydraulic connection between the two horizontal wells.

High flow rate, low horizontal filter section length, and low distance between the filter sections of the horizontal wells can lead to a thermal breakthrough. In the present example, this is the case at rate  $Q = 40 \text{ L s}^{-1}$  and filter section length below 250 m and at rate  $Q = 100 \text{ L s}^{-1}$  and filter section length below 500 m; in both cases the distance between the filter sections of the horizontal wells is 100 m. The thermal short circuit at the 'cold side' of ATES reduces pressure drawdown due to the lower dynamic viscosity of the hot fluid; the 'violet dotted line' in Fig. 13A corresponds to pressure drawdown of colder fluid, before the thermal short circuit occurs. No thermal breakthrough is observed under these conditions for horizontal wells with longer filter sections or with filter section distances of 400 m.

Similar effects can be observed in the numerical model at the 'hot side' of ATES: at injection start of  $80 \text{ }^\circ\text{C}$  hot water dynamic viscosity of aquifer-water is higher than towards the end of the injection. Thus, in the initial phase pressure buildup is higher than in the later course of the injection (not shown in Fig. 13A).

**Heating cycle** The heating cycle shows similar behavior (Fig. 13B): With increasing length of the horizontal wells' filter section induced pressure at the 'hot' and 'cold side' of ATES reduces. Increasing distance between the two filter sections of the horizontal wells (100 m vs. 400 m) results in higher pressure changes—with respect to the undisturbed pressure—on the 'hot' and the 'cold side' of ATES.

Reinjection at the 'cold side' of ATES is carried out with cooled water having the same temperature as the original, undisturbed aquifer. Thus, at the end of the heating cycle pressure buildup at the 'cold side' (Fig. 13B) corresponds as absolute value to the pressure drawdown at the end of the storage cycle at the 'cold side' of ATES (Fig. 13A).

Generally, pressure differences between the 'cold' and 'hot side' of ATES are higher at the end of the heating cycle than at the end of the storage cycle (Fig. 13A, B). Water temperature at the 'hot side' of ATES is decreasing during the heating cycle. At the end of the heating cycle temperature drops from  $80 \text{ }^\circ\text{C}$  to about  $50 \text{ }^\circ\text{C}$ , depending on rate, length of filter section, and distance between the horizontal wells in the aquifer. Thus, ATES is operated at the end of the heating cycle with lower temperatures at the

‘hot side’, causing higher dynamic viscosity and leading to higher pressure drawdown (Fig. 13B), in contrast to the end of the storage cycle, where temperature at the ‘hot side’ of ATEs is 80 °C (Fig. 13A).

The numerical model was used to calculate stored and produced thermal energies. Table 3 shows these results at the end of the 1st and at the end of the last (10th) cycle for different flow rates (10 L s<sup>-1</sup>, 40 L s<sup>-1</sup>, 100 L s<sup>-1</sup>), constant injection temperature of 80 °C at the ‘hot side’ of ATEs and constant re-injection temperature (temperature in the original, undisturbed aquifer) at the ‘cold side’ of ATEs, two different distances between the horizontal wells (100 m, 400 m), and different length of filter sections (250 m, 500 m, 1000 m).

Generally, with increasing flow rate (*Q*) more energy can be stored in and produced from the ATEs. However, during storage cycles at the ‘hot side’ of ATEs, short distances (*D*) between the horizontal wells and/or short filter section lengths (*L*) may result in thermal breakthrough to the ‘cold side’ of ATEs with the consequence that less thermal energy can be stored in the ‘warmer’ produced water. This effect is visible in Table 3, which compares the stored thermal energy after the 1st cycle with the last (10th) cycle. If both numbers are more or less equal, thermal breakthrough can be excluded. Table 3 shows as well that the efficiency of ATEs is increasing over time.

Stored and produced energies for the scenario with *Q*=40 L s<sup>-1</sup>, *D*=400 m and *L*=250 m (Table 3, 7th row, 4th and 7th column), calculated with the numerical model COMSOL, are in the same order of magnitude as the results from the numerical model OpenGeoSys (Table 2, 4th row, 3rd and 5th column), where filter section length of 210 m and a distance between the two inclined wells between 200 and 600 m are investigated.

The findings from the COMSOL model allow extending the earlier statement. Beside the increasing efficiency in each scenario from cycle to cycle (Figs. 12, 14) the conditions for low recovery factors can be quantified. Unfavorable conditions with 41% to 58% result from low flow rate (*Q*=10 L s<sup>-1</sup>) and low temperature difference, in combination with very long filter section (*L*=1000 m) and low distance between the two horizontal wells (100 m). The recovery factors for 400 m distance between the wells and otherwise same conditions are only slightly higher (c. 1%) (Fig. 14). Contrarily, highest recovery factors of 53% at the end of the 1st cycle and 75% at the last cycle are computed, when horizontal wells with very long filter sections (*L*=1000 m), very high flowrates (*Q*=100

**Table 3** Stored and produced thermal energy (GWh) at the end of the 1st and the last (10th) cycle for different rates (*Q*), distances between the horizontal wells (*D*) and filter section length (*L*)

<i>D</i> (m)	<i>L</i> (m)	Stored thermal energy (GWh)			Produced thermal energy (GWh)		
		Rate ( <i>Q</i> )			Rate ( <i>Q</i> )		
		10 L s <sup>-1</sup>	40 L s <sup>-1</sup>	100 L s <sup>-1</sup>	10 L s <sup>-1</sup>	40 L s <sup>-1</sup>	100 L s <sup>-1</sup>
100	250	6.6 / 6.3	26.0 / 23.8	57.8 / 52.1	3.1 / 4.3	12.5 / 16.6	29.1 / 36.0
	500	6.5 / 6.4	26.3 / 24.6	63.4 / 57.4	3.2 / 4.4	13.7 / 17.7	32.5 / 41.2
	1000	6.5 / 6.5	26.3 / 25.3	65.9 / 60.9	2.7 / 3.8	13.7 / 18.6	35.1 / 45.4
400	250	6.6 / 6.5	26.3 / 26.0	65.6 / 64.2	3.6 / 4.6	12.6 / 17.7	31.9 / 44.1
	500	6.6 / 6.5	26.3 / 26.1	65.7 / 64.9	3.4 / 4.5	14.1 / 18.6	33.3 / 45.9
	1000	6.5 / 6.5	26.3 / 26.0	65.7 / 65.2	2.8 / 3.8	13.6 / 18.2	33.0 / 45.0

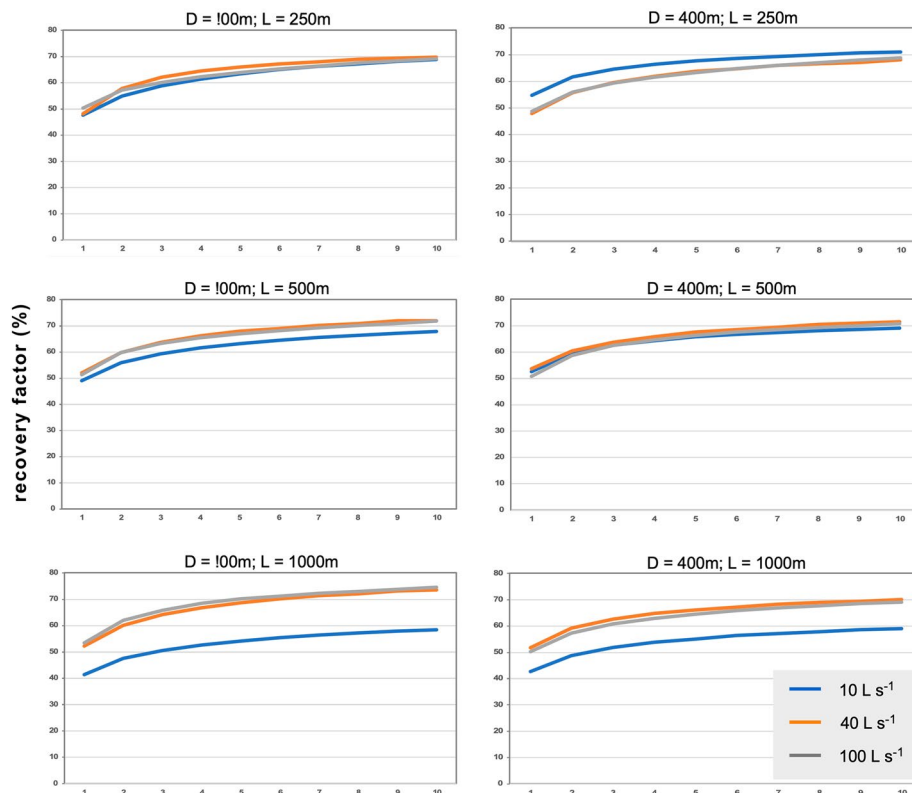


**Fig. 14** Recovery factors calculated with the COMSOL model for different scenarios, i.e., flow rates ( $10 \text{ L s}^{-1}$ ,  $40 \text{ L s}^{-1}$ ,  $100 \text{ L s}^{-1}$ ), filter section length  $L$  (250 m, 500 m, 1000 m), and distance between horizontal wells  $D$  (100 m, 400 m), and for 10 cycles

$\text{L s}^{-1}$ ), and 100 m distance between the wells are in operation, despite hydraulic connection between the wells. At higher distance ( $D=400 \text{ m}$ ) and thus lower hydraulic connection between the two wells the recovery factor reduces by 3.1–5.5% (Fig. 14). Thus, in these scenarios the thermal breakthrough has a positive effect with respect to the recovery factor. Highest recovery factors in the scenario with 400 m distance of the horizontal wells are calculated for a flow rate of  $Q=40 \text{ L s}^{-1}$  and a filter section length of  $L=500 \text{ m}$ , where no thermal breakthrough occurs.

The numerical modelling shows that recovery factors for flow rates of  $40 \text{ L s}^{-1}$  and  $100 \text{ L s}^{-1}$  are remarkably similar in each investigated scenario, also supporting the findings gained with the OpenGeoSys modeling (Figs. 12, 14). However, it should be noted, even if the recovery factors are very similar, the thermal energies produced are very different. Thus, the main important factor to produce high thermal energies is the amount of thermal energy injected during the storage cycle, i.e., the higher the temperature spread  $\Delta T$  the higher the produced thermal energy.

## Discussion

In a first step, the Petrel platform of Schlumberger Limited was used to construct a first large-scale subsurface model of the so called Freiburger Bucht, to get a better understanding of the complex geological conditions. To optimize the FE-network, a

significantly smaller, numerical 3D-model at the study site of the Fraunhofer IPM was extracted based on the main lithological and hydraulic findings and properties of the large-scale geological model.

The reference model, which is used in the first investigation scenarios with OpenGeoSys, is based on the input parameters given in Table 1 and considers a constant flow rate of  $10 \text{ L s}^{-1}$  and a temperature spread of 30 K. Aquifer storage operation is considered as an annual two-cycle process, with a storage cycle and a heating cycle. During the storage cycle, water heated up with surplus heat to a constant temperature of  $80 \text{ }^\circ\text{C}$  is pumped into the reservoir. Reinjection of the water in the heating cycle takes place under constant temperature of  $50 \text{ }^\circ\text{C}$ . Permeability variations are not explicitly presented, not to increase the number of variables unnecessarily. Instead, we show the influence of varying production- and injection rates. However, increasing the permeability by 100% will lead approximately to a halving of the maximum differential pressures and a reduction of permeability to 50% leads to an approximate doubling of the maximum differential pressures.

Variation of production- and injection-rate between  $5 \text{ L s}^{-1}$  and  $40 \text{ L s}^{-1}$  show, that in the reference model, i.e., inclined wells in the 150 m thick Buntsandstein aquifer with permeability of  $8.2 \times 10^{-14} \text{ m}^2$ , the chosen rate of  $10 \text{ L s}^{-1}$  is reasonable, because in case of increasing the rate the differential pressures between buildup and drawdown in the aquifer become irresponsibly high ( $\Delta p > 8 \text{ bar}$ ). In addition, with the selected doublet geometry (length of filter section: 210 m; distance between the two wells: 200 m at top Buntsandstein and 500 m at the base), a minimal thermal breakthrough is already evident at a flow rate of  $40 \text{ L s}^{-1}$ . However, the long-term behavior (10 storage-heating cycles) of the reservoir pressure is stable, regardless of the flow rate. Due to slightly increasing reservoir temperatures and thus lower fluid densities and viscosities, the differential pressure decreases slightly during the course of the long-term operation.

During each heating cycle temperature of the pumped water from well BS-North ('hot side' of ATEs) is decreasing, but in the course of the cyclic storage and heating operation (10 storage and heating cycles) the aquifer in the surroundings of well BS-North heats up and the usable temperature increases with each additional heating cycle, increasing the performance, efficiency, and energy yield of the aquifer storage from year to year. These results are in line with field data, which also show improvement of thermal recovery over several years (Molz et al. 1981; Sommer et al. 2014; Kranz et al. 2022). Additionally, the modeling results show, that regardless of the selected flow rate and temperature spread, slowly reduced performance-increases of the heating cycles are to be expected.

Another important result concerns the operation mode of the aquifer storage, in this case the temperature spread ( $\Delta T$ ). Injection temperature ( $80 \text{ }^\circ\text{C}$ ) into well BS-North ('hot side' of ATEs) during the storage cycle as well as production-/injection rate are kept constant ( $Q = 10 \text{ L s}^{-1}$ ) in this scenario. The influence of three different operation modes ( $\Delta T = 30 \text{ }^\circ\text{C}$ ;  $38.4 \text{ }^\circ\text{C}$ ;  $50 \text{ }^\circ\text{C}$ ) on the storage and heating cycle are investigated. The selected operation modes correspond to injection of water in well BS-South ('cold side' of ATEs) with higher, equal, and lower temperature compared to the undisturbed aquifer temperature. As a result, the low temperature spread ( $\Delta T = 30 \text{ }^\circ\text{C}$ ) leads to increasing temperature at the 'cold side' of the aquifer storage and realizable temperature spread during the storage cycle becomes slightly smaller

from year to year and, therefore, less energy can be stored in the ‘hot side’ of the aquifer storage. In contrast, high temperature spread ( $\Delta T = 50\text{ }^{\circ}\text{C}$ ) will lead to temperature decrease on the ‘cold side’ of the aquifer and thus, slightly more energy can be stored in the aquifer. Injection of water in well BS-South, with undisturbed aquifer temperature ( $\Delta T = 38.4\text{ }^{\circ}\text{C}$ ), will lead to constant energy storage conditions.

The performance of the aquifer storage depends primarily on two factors: (i) on the flow rate chosen for the injection and production of water into and from the reservoir; (ii) on the temperature spread ( $\Delta T$ ) chosen for the heat extraction in the heat exchanger in the operation mode. The amount of energy stored in the reservoir depends on flow temperature of BS-South (‘cold side’ of ATES) and the amount of energy extracted on the flow temperature of the BS-North (‘hot side’ of ATES).

Total energetic balance includes stored and produced energies for each storage-heating cycle. The efficiency of an aquifer storage, expressed by the recovery factor, is predominantly determined by the selected temperature spread ( $\Delta T$ ), whereas the influence of flow rate is only marginal. Generally, the recovery factor is increasing in the course of long-term operation. Higher rates lead to higher recovery factors. Highest efficiency can be obtained with reinjection temperatures below the undisturbed aquifer temperature. At the end of the long-term storage operation recovery factors of 60% ( $\Delta T = 30\text{ }^{\circ}\text{C}$ ), 72% ( $\Delta T = 38.4\text{ }^{\circ}\text{C}$ ), and 82% ( $\Delta T = 50\text{ }^{\circ}\text{C}$ ) are calculated for a flow rate of  $Q = 10\text{ L s}^{-1}$ . The modeled recovery factors are comparable with results of other studies (e.g., Molz et al. 1981; Schout et al. 2014; Sommer et al. 2014; Tordrup et al. 2016) and those measured in existing ATES like Berlin (77%), Rostock (55–70%), Neubrandenburg (72%), and Middenmeer (60–97%) (Sanner et al. 2005; Schmidt and Müller-Steinhagen 2005; Bloemendal et al. 2022).

To increase the flow rate parallel horizontal wells are as well incorporated into the numerical model of ATES, whereas calculation was executed with COMSOL. In contrast to our modelling concept considering two *parallel* horizontal wells (Fig. 6), Stricker et al. (2020) examined two horizontal wells pointing in the *opposite* direction (lateral distance of 500 m at the top of the reservoir), to avoid thermal interference between the wells. Our intention was, to investigate the efficiency, resp. the recovery factor, of the ATES and produced thermal energies by varying distances between the two parallel horizontal wells and lengths of the filter sections at different production rates and to determine the magnitude and effect of a potential thermal interference between the two parallel wells.

Calculations were done for different filter sections lengths (250 m, 500 m, 1000 m) of the wells on one hand and on the other hand for different distances (100 m and 400 m) between the horizontal wells in the aquifer, since due to Gao et al. (2017) suitable well distance decides the performance of the ATES system to a great extent. The numerical results show, that with increasing length of the horizontal wells’ filter section induced pressure at the ‘hot’ and ‘cold side’ of ATES reduces. Increasing distance between the two filter sections of the horizontal wells results in higher pressure changes—with respect to the undisturbed pressure—on the ‘hot’ and the ‘cold side’ of ATES. At the end of the heating cycle pressure buildup at the ‘cold side’ corresponds as absolute value to the pressure drawdown at the end of the storage cycle at the ‘cold

side' of ATES. Pressure differences between both wells are due to higher dynamic viscosity higher at the end of the heating cycle than at the end of the storage cycle.

### **Outlook**

Further investigation will be carried out on dynamic variation of heat production of various sources for storage, especially solar thermal energy production, waste heat of a nearby located chemical industry, or buffer storage for district heating. We intend to focus as well on dynamic variation of heat demand, as for example on the day-and-night cycles of heating. Thus, upcoming research will look at more realistic scenarios and the possibility of their implementation. Especially the trade-off between efficiency and thermal power of ATES-storage is of interest since the operation points for maximum efficiency and maximum power differ.

### **Conclusions**

3D numerical simulation of an ATES operation at the study site of the Fraunhofer IPM, i.e., seasonal storage and production of heat in the Buntsandstein aquifer via two inclined wells (BS-South, BS-North), was executed in a first step using the open-source software OpenGeoSys. The results were confirmed by the later use of the commercial software COMSOL. Special investigations concerning different configurations of the wells, especially horizontal wells, were carried out with COMSOL.

The produced thermal energy at the 'hot side' of ATES is in all investigated scenarios increasing from cycle to cycle, whereas main increases occur in the first few cycles. Thus, efficiency of ATES is generally increasing over time, for inclined and for horizontal wells. Also, stored and produced energies as well as recovery factors, calculated with OpenGeoSys and COMSOL, are for comparable scenarios in the same order of magnitude.

By implementing horizontal wells with sufficiently long filter sections, gentle pumping operation under moderate pressure differentials is possible. With increasing flow rate more energy can be stored in and produced from the ATES. However, during storage cycles at the 'hot side' of ATES, short distances between the horizontal wells and/or short filter section lengths may result in thermal breakthrough to the 'cold side' of ATES with the consequence that less thermal energy can be stored.

Recovery factors are higher when thermal breakthrough occurs, i.e., thermal breakthrough can have a positive effect with respect to the recovery factor. However, it should be noted, even if the recovery factors are very similar, the thermal energies produced may be very different. Thus, the main important factor to produce high thermal energies is the temperature spread and the flow rate.

Overall, the investigations have shown that it is possible to design aquifer-specific storage- and production performance by varying the spacing and filter length of the horizontal wells. Numerical modeling thus helps to reduce the exploration risk of an ATES project, since after drilling the first well, the modeling can be used to design the second well accordingly.



## Used software

- Petrel platform of Schlumberger Limited ([www.software.slb.com/products/petrel](http://www.software.slb.com/products/petrel))
- Program MeshIt (discretizing the 3D-model) by Cacace and Blöcher (2015)
- OpenGeoSys, open-source software, by Kolditz et al. (2012)
- COMSOL Multiphysics 6.1 ([www.comsol.com](http://www.comsol.com))

## Acknowledgements

We would like to thank both the Ministry of the Environment, Climate Protection and Energy Sector of Baden-Württemberg and the Projektträger Karlsruhe (PTKA) of Baden-Württemberg for funding of the project GtES, granted within the framework of BWPLUS (no.: L7516003-16004). Many thanks to Jörg Meixner for his support within the project GtES. For the provision of geological drilling profiles we would like to thank the State Office for Geology, Raw Materials, and Mining in Baden-Württemberg. We are also grateful for financial support of Herrenknecht Vertical GmbH and NG-Litef, Freiburg, within the framework of a PhD study.

## Author contributions

IS: conception of the paper, analysis and interpretation of geological and hydraulic data, supporting the numerical modeling, analysis and interpretation of the results, drafting and revision of the text; MJ: numerical modeling, analysis and interpretation of results, revision of the text; TK: discussion of results. All authors read and approved the final manuscript.

## Funding

Open Access funding enabled and organized by Projekt DEAL. No funding for this research. However, we used some data of a funded project mentioned in the acknowledgements.

## Availability of data and materials

All research data were presented or cited in this paper, most of which are freely available. The respective studies have been cited accordingly.

## Declarations

### Competing interests

The authors declare that they have no known competing financial interests or personal relationships that could have appeared to influence the work reported in this paper.

Received: 2 July 2023 Accepted: 3 November 2023

Published online: 02 December 2023

## References

- Bloemendal M, Hartog N. After the boom; evaluation of Dutch ATEs-systems for energy efficiency. *European Geothermal Congress*; 2016. p. 11. Strasbourg.
- Bloemendal M, Beernink S, Hartog N. Transition of ATEs to HT-ATEs: Field monitoring results of thermal impact and well temperature. *European Geothermal Congress*; 2022. 11. Berlin.
- Cacace M, Blöcher G. MeshIt—a software for three dimensional volumetric meshing of complex faulted reservoirs. *Environ Earth Sci*. 2015;74:5191–209. <https://doi.org/10.1007/s12665-015-4537-x>.
- Caliskan H, Dincer I, Hepbasli A. Thermodynamic analyses and assessments of various thermal energy storage systems for buildings. *Energy Convers Manag*. 2012;62:109–22.
- COMSOL Multiphysics® v. 6.1. [www.comsol.com](http://www.comsol.com). COMSOL AB, Stockholm, Sweden.
- Dashti A, Gholami-Korzani M, Geuzaine C, Egert R, Kohl T. Impact of structural uncertainty on tracer test design in faulted geothermal reservoirs. *Geothermics*. 2023. <https://doi.org/10.1016/j.geothermics.2022.102607>.
- Dèzes P, Schmid SM, Ziegler PA. Evolution of the European Cenozoic Rift System: interaction of the Alpine and Pyrenean orogens with their foreland lithosphere. *Tectonophysics*. 2004;389(1–2):1–33. <https://doi.org/10.1016/j.tecto.2004.06.011>.
- Dickinson JS, Buik N, Matthews MC, Sniijders A. Aquifer thermal energy storage: theoretical and operational analysis. *Géotechnique*. 2009;59(3):249–60.
- Dincer I. Thermal energy storage systems as a key technology in energy conservation. *Int J Energy Resour*. 2002;26(7):567–88.
- Dinkelmann D, van Bergen J-D. Evaluation of the country-wide potential for High-Temperature Aquifer Thermal Energy Storage (HT-ATEs) in the Netherlands. *European Geothermal Congress*. 2022; p. 9. Berlin.
- Dinkelmann D, Carpentier S, Koenen M, Oerlemans P, Godschalk B, Peters E, Bos W, Vrijlandt M, van Wees J-D. High temperature aquifer thermal energy storage performance in Middenmeer, the Netherlands: thermal monitoring and model calibration. *European Geothermal Congress*; 2022. p. 10. Berlin.
- do Guimarães LN, Gens A, Sánchez M, Olivella S. THM and reactive transport analysis of expansive clay barrier in radioactive waste isolation. *Commun Numer Methods Eng*. 2006;22(8):849–59. <https://doi.org/10.1002/cnm.852>.
- Doughty C, Hellström G, Tsang CF. A dimensionless parameter approach to the thermal behavior of an aquifer thermal energy storage system. *Water Resour Res*. 1982;18(3):571–87.

- Eren T, Polat C. Well efficiency assessment in geothermal fields for horizontal drilling. *J Petrol Sci Eng.* 2019;178:904–20. <https://doi.org/10.1016/j.petrol.2019.04.015>.
- Fleuchaus P, Godschalk B, Stober I, Blum P. Worldwide application of aquifer thermal energy storage—a review. *Renew Sustain Energy Rev.* 2018;94:861–76.
- Frey M, Bär K, Stober I, Reinecker J, van der Vaart J, Sass I. Assessment of deep geothermal research and development in the Upper Rhine Graben. *Geotherm Energy.* 2022;10:18. <https://doi.org/10.1186/s40517-022-00226-2>.
- Gao L, Zhao J, An Q, Wang J, Liu X. A review on system performance studies of aquifer thermal energy storage. *Energy Procedia.* 2017;142:3537–45.
- Geyer OF, Gwinner MP. Geologie von Baden-Württemberg.- neu bearbeitete Auflage von Geyer M, Nitsch E, Simon T (Hrsg.). Schweizerbart'sche Verlagsbuchhandlung (Nägele u. Obermiller), Stuttgart; 2011.
- Gholami Korzani M, Held S, Kohl T. Numerical based filtering concept for feasibility evaluation and reservoir performance enhancement of hydrothermal doublet systems. *J Petrol Sci Eng.* 2020;190: 106803.
- Groschopf R, Kessler G, Leiber J, Maus H, Ohmert W, Schreiner A, Wimmenauer W, Albiez G, Hüttner RU, Wendt O. Erläuterungen zur Geologischen Karte von Freiburg im Breisgau und Umgebung 1 : 50 000. Geologisches Landesamt, 3. erg. Aufl.—IV, 364 S., Freiburg; 1996.
- Haehnlein S, Bayer P, Blum P. International legal status of the use of shallow geothermal energy. *Renew Sustain Energy Rev.* 2010;14(9):2611–25. <https://doi.org/10.1016/j.rser.2010.07.069>.
- Homilius J, Schreiner A. Geoelektrische Untersuchungen in der Freiburger Bucht. *Geol Jb.* 1991;E48:43–70.
- Illies JH, Fuchs K, editors. Approaches to Taphrogenesis. Stuttgart: Schweizerbart; 1974.
- Jäggle M, Meixner J, Stober I, Kohl T. Machbarkeitsstudie zur Kopplung solarthermischer Nahwärme mit einem tiefen Geothermalen Energiespeicher (GTES) in Baden-Württemberg. Verbundprojekt des Landes Baden-Württemberg BWPLUS, Abschlussbericht: L75 16003–16004, 97 S. 2018; Karlsruhe.
- Jodocy M, Stober I. Geologisch-geothermische Tiefenprofile für den südlichen Teil des Oberrheingrabens in Baden-Württemberg. *Z Geol Wiss.* 2010;38:3–25.
- Kolditz O, Bauer S, Bilke L, Böttcher N, Delfs JO, Fischer T, Görke UJ, Kalbacher T, Kosakowski G, McDermott CI, Park CH, Radu F, Rink K, Shao H, Shao HB, Sun F, Sun YY, Singh AK, Taron J, Walther M, Wang W, Watanabe N, Wu Y, Xie M, Xu W, Zehner B. OpenGeoSys: an open-source initiative for numerical simulation of thermo-hydro-mechanical/chemical (THM/C) processes in porous media. *Environ Earth Sci.* 2012;67:589–99. <https://doi.org/10.1007/s12665-012-1546-x>.
- Kranz S, Frick S. Efficient cooling energy supply with aquifer thermal energy storages. *Appl Energy.* 2013;109:321–7. <https://doi.org/10.1016/j.apenergy.2012.12.00>.
- Kranz S, Blöcher G, Francke H, Saadat A. ATEs design aspects and optimized system integration. European Geothermal Congress; 2022. Berlin.
- Lee K-S. A review on concepts, applications, and models of aquifer thermal energy storage systems. *Energies.* 2010;3:1320–34. <https://doi.org/10.3390/en3061320>.
- Li G. Sensible heat thermal storage energy and exergy performance evaluations. *Renew Sustain Energy Rev.* 2016;53:897–923.
- Molz FJ, Parr AD, Andersen PF. Thermal energy storage in a confined aquifer: second cycle. *Water Resour Res.* 1981;17(3):641–5. <https://doi.org/10.1029/WR017i003p00641>.
- Permann CJ, Gaston DR, Andrs D, Carlsen RW, Kong F, Lindsay AD, Miller JM, Peterson JW, Slaughter AE, Stogner RH, Martineau RC. MOOSE: enabling massively parallel multiphysics simulation. *SoftwareX.* 2020;11: 100430.
- Rabbinov RT, Unarov GY, Zakhidov RA. Storage of solar energy in sandy-gravel ground. *Geliotekhnika.* 1971;7(5):57–64.
- Rupf I, Nitsch E. Das Geologische Landesmodell von Baden-Württemberg: datengrundlagen, technische Umsetzung und erste geologische Ergebnisse. *Informationen* 21. 2008; Landesamt für Geologie, Rohstoffe und Bergbau (LGRB), Freiburg.
- Sanner B, Kabus F, Seibt P, Bartels J. Underground thermal energy storage for the German parliament in Berlin, system concept and operational experiences. *Proc World Geotherm Congr Antalya.* 2005;1438:1–8.
- Sauty JP, Gringarten AC, Fabris NH, Thiery D, Menjoz A, Landel PA. Sensible energy storage in aquifers: field experiments and comparison with theoretical results. *Water Resour Res.* 1982;18(2):253–65.
- Schmidt T, Müller-Steinhagen H. Erdsonden- und Aquifer-Wärmespeicher in Deutschland. OTTI Proforum Oberflächennahe Geothermie. 2005; 12 S., Regenstauf, 14.–15. April.
- Schout G, Drijver B, Gutierrez-Neri M, Schotting R. Analysis of recovery efficiency in high-temperature aquifer thermal energy storage: a Rayleigh-based method. *Hydrogeol J.* 2014. <https://doi.org/10.1007/s10040-013-1050-8>.
- Schulz R, Schellschmidt R. Das Temperaturfeld im südlichen Oberrheingraben. *Geol Jahrb.* 1991;E48:153–65.
- Shiozawa S, McClure M. EGS designs with horizontal wells, multiple stages, and proppant. Proceedings, Thirty-Ninth Workshop on Geothermal Reservoir Engineering. Stanford University, SGP-TR-202, Stanford; 2014.
- Sommer WT, Doornenbal PJ, Drijver BC, Gaans PFM, Leusbrock I, Grotenhuis JTC, Rijnaarts HHM. Thermal performance and heat transport in aquifer thermal energy storage. *Hydrogeol J.* 2014;22:263–79. <https://doi.org/10.1007/s10040-013-1066-0>.
- Stephanson O. Coupled thermo-hydro-mechanical-chemical processes in geo-systems: fundamentals, modelling, experiments and applications. Elsevier Geo-Eng Book Ser. 2004;2:832.
- Stober I, Bucher K. Hydraulic and hydrochemical properties of deep sedimentary aquifers of the Upper Rhine Graben. *Europe Geofluids.* 2015;15:464–82. <https://doi.org/10.1111/gfl.12122>.
- Stober I, Bucher K. Geothermal energy, from house heating applications to electrical power production. 2nd ed. Springer; 2021. p. 390.
- Stober I, Jodocy M. Eigenschaften geothermischer Nutzhorizonte im baden-württembergischen und französischen Teil des Oberrheingrabens. *Grundwasser.* 2009;14:127–37. <https://doi.org/10.1007/s00767-009-0103-3>.
- Stricker K, Grimmer JC, Egert R, Bremer J, Gholami Korzani M, Schill E, Kohl T. The potential of depleted oil reservoirs for high-temperature storage systems. *Energies.* 2020;13:6510. <https://doi.org/10.3390/en13246510>.
- Tordrup KW, Poulsen SE, Bjørn H. An improved method for upscaling borehole thermal energy storage using inverse finite element modelling. *Renew Energy.* 2016. <https://doi.org/10.1016/j.renene.2016.12.011>.
- Villingner E. Freiburg im Breisgau—Geologie und Stadtgeschichte. *Informationen* 12, Landesamt für Geologie, Rohstoffe und Bergbau (LGRB); 1999. p. 60, Freiburg

- Wesselink M, Liu W, Koornneef J, van den Broek M. Conceptual market potential framework of high temperature aquifer thermal energy storage—a case study in the Netherlands. *Energy*. 2018;147:477–89.
- Ziegler PA. European Cenozoic rift system. *Tectonophysics*. 1992;208(1):91–111. [https://doi.org/10.1016/0040-1951\(92\)90338-7](https://doi.org/10.1016/0040-1951(92)90338-7).

### **Publisher's Note**

Springer Nature remains neutral with regard to jurisdictional claims in published maps and institutional affiliations.